RSC Publishing Journal of Materials Chemistry B

Striped, bioactive Ce-TiO2 material with peroxynitrite-scavenging activity

Journal:	*Journal of Materials Chemistry B*
Manuscript ID:	TB-ART-11-2013-021556
Article Type:	Paper
Date Submitted by the Author:	04-Nov-2013

Complete List of Authors:	Gravina, Anabela; Universidad Nacional del Sur, Chemistry Ruso, Juan; University of Santiago de Compostela, Applied Physics Laiuppa, Juan; Universidad Nacional del Sur, Santillán, Graciela; Universidad Nacional del Sur, Marco-Brown, José; Universidad de Buenos Aires, Department of Inorganic Chemistry, Analytics and Physical Chemistry D'Elía, Noelia; Universidad Nacional del Sur, Chemistry Messina, Paula; Universidad Nacional del Sur, Chemistry Department

Striped, bioactive Ce-TiO_2 material with peroxynitrite-scavenging activity

*A. Noel Gravina[a], Juan M. Ruso[b], Juan A. Laiuppa[c], Graciela E. Santillán[c], Jose L. Marco-Brown[d], Noelia L. D'Elia[a], Paula V. Messina [a]**

(a) Department of Chemistry, Universidad Nacional del Sur, 8000, Bahía Blanca, Argentina. INQUISUR-CONICET (b) Soft Matter and Molecular Biophysics Group, Department of Applied Physics, University of Santiago de Compostela, Santiago de Compostela, 15782, Spain. (c) Department of Biology, Biochemistry and Pharmacy, Universidad Nacional del Sur, (8000) Bahía Blanca, Argentina (d) Department of Inorganic Chemistry, Analytics and Physical Chemistry, INQUIMAE, FCEN, Universidad de Buenos Aires, Pabellón II, C1428EHA, Buenos Aires, Argentina.

* Author to whom correspondence should be addressed. Tel: +54 291 4595159. Fax: +54 291 4595160. Electronic mail: pmessina@uns.edu.ar.

Abstract. Controlling aligned fiber micro-architectures to simulate extracellular matrix inducing important biological functions is a key challenge in regard to successful tissue regeneration. Here we present a bottom-up microemulsion mediated strategy to obtain highly bioactive and biocompatible, striped Ce-TiO_2 nano-crystalline superstructures with $ONOO^-$ scavenging activity. The employment of a bulkier organic ceria precursor on the material synthesis has several concurrently effects: (I) influencing the interfacial microemulsion droplet elasticity to create an aligned distribution of prismatic anatase nano-particles causing the final lined morphology; (II) stabilizing the anatase active phase in a fine dispersed state and improving it resistance to the thermal anatase-rutile conversion; (III) indirectly favoring the rapid formation on the material surface of a hydroxyapatite layer composed of spherical-like globules with 3-5 μm in diameter essential for bone-bonding; and finally (IV) accelerating the $ONOO^-$ degradation to a less harmful species NO_2^- and O_2.

Keywords: Striped material, anatase, peroxynitrite, hydroxyapatite, microemulsion.

1. Introduction

In the science of bone-tissue biomaterials it is a primordial challenge to make implantable devices that have simultaneously bioactive and biocompatible properties[1]. Scaffolds with novel biofunctionality levels that attempt to restore nanoscale morphology and biofactor cues of the extracellular matrix (ECM) are emerging as striking biomimetic candidates[2].

The importance of the implant surface with respect to the tissue reaction has been recognized with regard to maintain a stable interface between the material and the host tissue[3]. Commercially pure titanium and titanium alloys including Ti6Al4V that possess high oxidation number and high acidity are widely used in manufacturing of dental and orthopedics implants. However, the experimental results obtained by a variety of researchers[4] demonstrated that the bioactivity of titanium and titanium surfaces is not high enough to induce the direct growth of bone tissue and a good fixation before several months[3]. Owing to the reasons listed before, that many efforts of the scientist community were directed to the modification of metal surface topographies to control tissue-implant interactions and shortening the time of bone fixation[3, 4]. In this regard, it is reasonable to expect that an engineered material scaffold mimicking ECM will play a similar role to promote tissue regeneration *in vitro* as native ECM does *in vivo*. In spite of the astounding diversity of ECM structures caused by different bio-macromolecules and the way they are organized, a well-known feature of native ECM is the nanoscale dimensions and the fibrous morphology of their physical structure[5]. Since 1960s, researchers claim that nanoscale features influence cell behavior[6]. Recently, nano-phase materials modified to simulate not only the nanometer dimension but also the fibrous aspect found in bone ECM were produced[7]. Scaffolds with nano-fibrous structure adsorb highly amounts of serum proteins[8, 9] and also selectively enhance osteoblastic cell attachment[1, 7, 9] compared with solid walls scaffolds.

Another important point to take into account during the design of an implantable material is the possible host tissue damage. The process of implantation of any material leads to the creation of a wound at the implantation site. It is now established that a balance between bio-available nitric oxide (NO) concentration and the level of both reactive oxygen and nitroxide species in wounds may be crucial in the repairing process[10]. The oxidants play an important role in wound repair healing providing signaling and defense against microorganism[11, 12]. However, these oxidants have to be detoxified in order to prevent damage of host cells. The antioxidant defense system involves reduction (scavenging) and/or dismutation of O_2^- and $ONOO^-$ and their protonated form[10]. When the antioxidant defense system fails to eliminate the oxidants the alteration in homeostasis leads to oxidative stress which favors the damage of the cells[11, 12]. Cerium oxide (ceria) nanoparticles have been shown to possess a substantial oxygen storage capacity via the interchangeable surface reduction and oxidation

of cerium atoms, cycling between the Ce^{4+} and Ce^{3+} redox states[13]. Biological uses of CeO_2 nanoparticles have centered on their ability to scavenge free radicals under physiological conditions[14]. This catalytic behavior is comparable with those observed for superoxide dismutase [15] and catalase[16]. Because of its unique redox properties, nanoceria has been tested in both animal and cell culture models to determine its ability to protect against oxidative stress[17]. The application of ceria nanoparticles in the treatment of spinal cord injury and other central nervous system-based neuron degenerative diseases has proven the biological importance of nanoceria[13]. For example, glutamate induced excitotoxicity was reduced in HT22 neuronal cell model after treatment with cerium or yttrium nanoparticles[18] and the treatment of adult rat neurons with 10 nM concentration of nanoceria resulted in a decrease in cellular senescence after 30 days[19]. In addition, the application of nanoceria to transgenic mice expressing high levels of chemoattractant MCP-1 showed reduced inflammation and cell death in a cardiovascular disease model[20]. Ceria nanoparticles can also prevent retinal degeneration by intracellular peroxide molecules[21].

In the present study, we report the use of a simply bottom-up reverse microemulsion method to control the morphology of Ce doped TiO_2 crystals during hydrothermal synthesis at 100ºC. We conducted phase behavior measurements on several systems to identify the properly synthesis conditions. Under specific synthesis conditions a striped Ce-doped TiO_2 material was obtained. The material was designed to merge fibrillar nanoscale morphology and the scavenging properties of Ce on a TiO_2 substrate.

As it was mentioned above, the role of the materials surface properties in cell guidance are well known, but how these aspects affect their bioactivity is still under investigation. Thus, we investigated the effect of surface area, morphology and roughness on the material bioactivity and biocompativility. Simultaneously we studied the effect of ceria doping in the ability of the materials to interact with oxygen and nitrogen reactive species. The results obtained give a step forward to the construction of engineered scaffolds designed to mimic the structural and biological functions of native extracellular matrix in calcified tissues.

2. Experimental Section

2.1 Reagents

Hexadecyl-trimethyl ammonium bromide (CTAB, MW = 364.48 g mol^{-1}, 99% Sigma), n-heptane (MW = 100.21 g mol^{-1}, δ = 0.684 g cm^{-3}, Merck), butyl alcohol (ButOH, MW = 74.12 g mol^{-1}, δ = 0.810 g cm^{-3}, Merck,), cerium valerate ($Ce(Val)_3$, MW = 443.1 g mol^{-1}) and titanium (IV) isopropoxide (TTIP,

Ti (IV)$(OiPr)_4$, MW = 284.22 g mol^{-1}, δ= 0.960 g cm^{-3}, 97% Aldrich) were used without further purification. For microemulsion preparation, only triple-distilled water was used.

2.2 Material synthesis.

Selected synthesis conditions were carefully investigated in previous works[22-24].

2.2.1 CeO_2 nanoparticles: For CeO_2 nanoparticles synthesis a double-microemulsion method was used[25]. Microemulsion ***A*** containing 12.8% of CTAB, 9.6% of 1-butanol, 44.7% of oil phase, 31.9% of aqueous phase and 1% of $Ce(Val)_3$ was mixed with a microemulsion ***B*** containing 12.78% of CTAB, 9.58% of 1-butanol, 44.71% of oil phase, 31.93% of aqueous phase and 1% of NaOH using a magnetic stirrer for 1h. The resulting microemulsion developed a yellowish hue, indicating the formation of CeO_2 nanoparticles, which were extracted by centrifuging at 10000 rpm for 10 min. The CeO_2 nanoparticles were then washed with ethanol and stored as dispersion in ethanol.

2.2.2 TiO_2 material: The pure TiO_2 material (MI) was prepared using a single microemulsion method[25]. Final microemulsion systems of S_0 = 13, W_0 = 51, Ti^{4+}/ surfactant = 1 and ButOH /surfactant = 8 were prepared, where W_0 is the ratio of water to surfactant molar concentrations and S_0 is the ratio of oil to surfactant molar concentration. During the synthetic procedure a microemulsion ***C*** containing: 14.6% of CTAB, 23.6% of 1-butanol, 25.3% of oil phase, and 36.5% of aqueous phase was mixed with a solution ***D*** formed by the dissolution of 2 mL TTIP in 5.07 mL n-Heptane without stirring and left to equilibrate for 20 minutes to follow the reaction:

Ti (IV)$(OiPr)_4 + 2\ H_2O \leftrightarrows TiO_2 + 4$ HOiPr (1)

2.2.3 Ce-TiO_2 material: A similar procedure was employed to prepare two different Ce-TiO_2 materials (MII and MIII). For the preparation of MII and MIII 2.72 mg of Ce $(Val)_3$ or 1mL of CeO_2 nanoparticles synthesized according to the previous descript procedure were added respectively to microemulsion ***C*** before mixing with solution ***D*** (**item 2.2.2**). For both TiO_2 and Ce-TiO_2 materials, the resulting gels were left for 24h in an autoclave at 100ºC. The obtained materials were filtered, washed with triple-distilled water and left to dry at room temperature. Finally, they were calcined for 7h at 650ºC in an air flux.

2.3 Material characterization.

2.3.1 Field emission scanning electron microscopy (FE-SEM). Surface morphology was evaluated using a field emission scanning electron microscope (ZEISS FE-SEM ULTRA PLUS). To acquire all the SEM images a Secondary Electron Detector (In lens) was used. The accelerating voltage (EHT) applied was 3.00 kV with a resolution (WD) of 2.1 nm. Local compensation of charge (by injecting

nitrogen gas) was applied avoiding the sample. Quantitative information about surface elemental composition was determined by the associated X-ray energy-dispersive (EDX) spectrometer. The topography of samples was quantified from SEM microphotographs using different software packages[26], uncertainty of 5%.

2.3.2 High resolution transmission electron microscopy (HTEM). High resolution transmission (H-TEM) microphotographs were taken using a Libra 200 FE OMEGA transmission electron microscope operated at 200 kV with magnification of 1000000x. Observations were made in a bright field. Powdered samples were placed on carbon supports of 2000 mesh.

2.3.3 Nitrogen adsorption isotherms. The nitrogen adsorption isotherms at 77.6 K were measured with a Micrometrics Model Accelerated Surface Area and Porosimetry System (ASAP) 2020 instrument. Each sample was degassed at 373 K for 720 min at a pressure of 10^{-4} Pa. To determine the Brunauer-Emmet-Teller (BET) surface area, S_{BET}, the nitrogen molecules diameter is taken as 0.43 nm, calculated by assuming the closest packing spheres[27], and the area per molecule a_m = 0.1620 nm[228, 29]. The pore diameter and the pore size distribution were calculated from the adsorption branch of the isotherm by applying the BJH method[28, 29].

2.3.4 X-ray powder diffraction. Powder X-ray diffraction (XRD) data were collected with a Philips PW 1710 diffractometer with Cu K_α radiation (λ = 1.5418 nm) and Graphite monochromator operated at 45 kV; 30 mA and 25ºC. The mean crystalline size (δ) of the particles was calculated from XRD line broadening measurement using the Scherrer equation[22]:

$$\delta = \frac{0.94\lambda}{\beta \cos\theta}$$

λ is the wavelength (Cu K_α), β is the relative peak broadening, calculated as $\beta^2 = \beta_{exp}^2 - \beta_{ref}^2$ where β_{exp} and β_{ref} are half widths at maxima observed on a given sample and on a reference material which is ideally crystalline, respectively[30].

The rutile to anatase ratio (F_r) was computed from the XRD intensity data by the following equation[31]:

$$F_r = 1 - \left(1 + 1.265 \frac{I_{rutile\ (110)}}{I_{anatase\ (101)}} \right)$$

2.4 Bioactivity assay.

To perform the bioactivity assay, the material was kept in contact with simulated body fluid (SBF) following the standard procedure described by Kokubo *et al.*[32], which has a composition and ionic concentration similar to that of human plasma, containing Na^+ (142.0 mM), K^+ (5.0 mM), Mg^{2+} (1.5

mM), Ca^{2+} (2.5 mM), Cl^- (148.8 mM), HCO^{3-} (4.2 mM), HPO_4^{-2} (1.0 mM) and SO_4^{-2} (0.5mM). The synthesized materials were soaked in 1.5 SBF at 37ºC for periods of 1, 3, 6, 10, 15, 20, 30, 65 days, the specimens were removed from fluid, rinsed with distilled water and dried. The temperature (37ºC) was maintained by placing the samples in a thermostatic bath throughout the experiment.

2.5 $ONOO^-$ decay.

Peroxynitrite ($ONOO^-$) solutions were prepared by mixing acidified hydrogen peroxide with nitrite (reaction 2) in a simple flow system, and quenching ONOOH with alkaline solution (reaction 3) accordingly to Beckman *et al*.[33] using the improved method of Saha *et al.* [34] for the generation of maximum yield of peroxynitrite with minimum amounts of residuals H_2O_2 and nitrite.

$$H_2O_2 + HNO_2 \rightarrow ONOOH + H_2O \quad (2)$$

$$ONOOH + OH^- \rightarrow ONOO^- + H_2O \quad (3)$$

The solutions of peroxynitrite can be kept at -22°C, where peroxynitrite gradually decomposes with a half life of 1 to 2 weeks[33]. Nevertheless, we used a freshly prepared solution for each experiment. For spectrophotometric decay studies 100 μL of the above obtained peroxynitrite solution (pH = 13.3) was added into a 1 mL quartz cuvette with a 1 cm path length and diluted with 900 μL of 100 mM sodium potassium phosphate buffer (pH = 7.4) or 900 μL of tri-distilled water as required. Each sample was analyzed for a total of 3500 seconds with a cycle time of 0.5 seconds at a wavelength of 302 nm using a JASCO V-630 bio spectrophotometer provided with a temperature controller (ETCS-761 JASCO). Absorbance was normalized by subtracting the final absorbance from initial absorbance and dividing by the amplitude as described Quijano *et al*.[35]. The experiments were performed three times with and without the presence of 10 mg of each material.

2.6. Osteoblast isolation

Calvarial osteoblasts were obtained from 5-day-old neonatal rats which were sacrificed by fast decapitation. All procedures were carried out in conformity with the Guide for the Care and Use of Laboratory Animals published by the US National Institutes of Health (NIH Publication No. 85-23, revised 1996). Briefly, calvarias were incubated in phosphate buffer saline (PBS) containing 4 mM EDTA at 37°C for two 10-min periods, and the supernatants were discarded. Subsequently, calvarias were rinsed in PBS and submitted to digestion in PBS containing 200 U/ml collagenase for four 15-min

periods. Cells released during the first digestion were discarded, and those released during the subsequent digestions were spun down, collected and combined after centrifugation during 10 min at 1500 rpm. Then, cells were cultured at 37°C in α-MEM supplemented with 15% FBS, 1% penicillin and streptomycin under humidified air (5.5% CO2). After 24 h, the medium was replaced by α-MEM supplemented with 10% FBS, 1% penicillin and streptomycin, and the cells were cultured until ~80 % of confluence (2-3 days). Then, the cells were frozen in liquid nitrogen until their use.

2.7 Osteoblast culture and treatment

Calvarial osteoblasts seeded in 48-well plates were cultured for 1 day in α-MEM supplemented with 10% FBS, in a humidified atmosphere (5.5% CO2) at 37°C. Then, 50 μg per well of nano-particles from each compound were added on adhered cells and continued incubating for 24 or 72 h. Cells incubated in the same conditions without nano-particles were taken as controls.

2.8 Cell viability and statistical analysis

After treatments, the controls and treated cells with the nano-particles were washed with PBS buffer. Then, the cells were detached using 0.25% trypsin in PBS (25μl/well) and stopped it with 100 μl of α-MEM supplemented with 10% FBS. Follow, 10 μl/well of 0.1% Trypan Blue dye was added and cells were counted in a haemocytometer. The percent of cells that excluded the stain (viable cells) respect to the total cells (viable + non-viable cells) was obtained. Statistical significance of data was evaluated using Student's t-test and probability values above 0.05 ($P > 0.05$) were considered non significant[36]. Quantitative data are expressed as means ± standard deviation (SD) from the indicated set of experiments.

2.9 Cell morphology analysis

Control and treated cells with 50 μg per well of nano-particles from each compound for 72 h were used to evaluate the cell morphology. The samples were fixed with methanol and stained by Giemsa[37] stain

3. Results and discussion

3.1 Ce-TiO_2 materials

3.1.1 Microemulsion-mediated hydrothermal synthesis: effect on the material final striped morphology.

TiO_2 and Ce-TiO_2 materials were generated in a reverse microemulsion-mediated hydrothermal synthesis; the surfactant-stabilized water nano-droplets play the role of nano-reactors to control the particles size and shape during a hydrothermal treatment at 100ºC. **Figures 1 and 2** shows the SEM microphotographs of TiO_2 and Ce-TiO_2 synthesized materials. All samples are composed of small prismatic nano-particles of about 30-50 nm length. The presence of Ce-atoms during the synthesis of the material results in a decrease in the size of the particle. The incorporation of CeO_2 nanoparticles ($d \approx 5$ nm [23]) to the synthesis mixture, did not cause any alteration to the final product morphology, **figure 1,** so MI and MIII present a similar undefined morphology. However, in MII prismatic nanoparticles are organized forming a striped topography of 10μm length and 0.25μm diameter aligned fibers, **figure 2**. Size distribution histograms are shown in **ESI**. The stability of the microemulsion, which affects the success of the synthesis, depends on several process conditions: the water to surfactant molar ratio (W_0); the oil to surfactant molar ratio (S_0); the kind and content of stabilizing agent; the precursor concentration in the solution and the mixing speed. The fine combination of the above mentioned parameters exert a delicate control over micro-droplets interfacial elasticity, the exchange of reactive species and the final material morphology[38]. Cetyl trimethylammonium bromide provides a very flexible film, which gives rise to a high exchange dynamic of the micelles[39]. Therefore, the dynamic nature of the reverse microemulsion droplets swap plays a key role in the formation of the last material shape. This, in turns, is closely related to the rigidity of the nano-droplet oil-water interface. In previous works[22-24] we assessed the effect of interfacial micro-droplet rigidity in the final nano-material morphology. Under hydrothermal conditions, the formation of different inorganic structures goes via an oriented aggregation mechanism[23, 24]. We signaled the need of an inflexible interface to conduct the formation of elongated structures during a hydrothermal-mediated microemulsion process. When the film is flexible, by subjecting the microemulsion to the effect of the hydrothermal treatment, reverse micelles brake as shown in the oriented aggregation mechanism[38] and due to their flexible interface, the nano-droplets merge adopting a bicontinuous structure[23, 24]. As a result, the final obtained material showed a non-defined or a bicontinuous structure. However, when the film seems to be rigid enough, the formation of interconnected channels is avoided and the inorganic material growing inside the droplets lead to the formation of lengthened structures. During the synthesis of MII material, it is possible that the presence of $Ce(Val)_3$ bulkier groups must influence the interfacial organization by affecting the compactness of the surfactant film and its temporal stability. It might also modify the packing parameter and, in turn, manipulate the radius of curvature of the microemulsion droplet in a way that causes an increase of the oil-water interface stiffness. If the molecules are allowed to adjust

their area per molecule depending on the curvature, the interface will be less rigid upon bending, **scheme 1**. This interfacial change seems to be sufficient to cause an elongated association of nanoparticles; but not enough to succeed the formation of fibrillar structures. A similar effect was observed during the preparation of Ce-doped SiO_2 materials by an analogous procedure[23].

Another important point to analyze, which is related to the final material morphology, is the inorganic precursor poly-condensation. The hydrolyses of titanium alkoxides are very complex[40]. These reactions produce polycondensates which their chemical compositions are a function of their physical size and polymeric morphology. For TTIP hydrolysis, Park *et al*.[41] had found that the reaction occurred via an associative mechanism and had detected an intermediate with a coordination number of five –OR groups. Thermodynamic data shows a high activation enthalpy in combination with small activation entropy values. Those facts are linked to the difficulty of weakening the leaving group bond, and the complexity of the bond formation for the entering group[41]. The microemulsion systems prepared have a W_0 value 4 and 51 times higher than the S_0 and the Ti^{4+}/surfactant ratio respectively. The co-surfactant/surfactant ratio is about 8, alongside water/Ti^{4+} and oil/Ti^{4+} ratio are 40 and 10 times larger than Ti^{4+}/surfactant ratio. Under these experimental conditions, there are a slow diffusion of Ti^{4+} ions through continuous organic phase inside the aqueous microemulsion droplets and a slower hydrolysis of TTIP in comparison with the microemulsion interdroplet exchange rate[38]. The oxide network extends as far as the hydrolysis conditions permit[40] limited by microemulsion confinements and related, as mentioned above, to interfacial elasticity. In our case, the production of isopropanol (reaction 1) does seem to have a relevant effect on microemulsion systems, probably because most of -OR groups seem to be located inside microemulsion droplet core forming part of the TTIP poly-condensation product[41].

3.1.2 Structural characterization: microcrystalline and topographical analysis.

Bone formation around the implant is an intricate process, and it is not completely understood. Simultaneously with the patient's metabolism, physicochemical and topographical surface characteristics are some of the most influential factors in the improvement of osseo- integration[42]. The crystal structure of the synthesized materials before and after annealing has been confirmed by X-ray diffraction, **ESI,** and high resolution electron microscopy, **figure 3**. The diffraction patterns clearly indicates that all samples before annealing are constituted by a pure anatase phase (tetragonal, I41/amd, JCPDS cards 21-1272). In a previous work, we have demonstrated that the presence of RSO^{3-} anions in water/AOT/ n-heptane microemulsion leads to the inhibition of some crystal facets growth and leads to the formation of small-sized anatase nanocrsytallites embryos with a characteristic shape (or facets

exposed to the surface)[43]. Here with an interfacial co-surfactant/surfactant molar ratio = 8, probably the –OH groups of butanol can act likewise. It is known that several ligands that contains $–COO^-$, –CO and ROH^- groups are stronger field ligand than Cl- and OH- ions and substitute them in the $(Ti(OH)_xCl_y)^{2-}$ complexes [44]. Furthermore, Porta et al.[45] emphasized the possibility that 1-butanol behaves as capping agent during the preparation of Au nanoparticles. After calcination at 650ºC, MI is partially transformed in TiO_2 rutile in accordance with anatase to rutile transition that occurs at 600ºC and 1 atm[46], while MII and MIII continued being anatase, **ESI**. The absence of diffraction peaks at 31º shows that always the samples were free from TiO_2 brookite structures. No traces of diffraction peaks due to cerium oxide were detected. This is attributed to the small amount, the high area of distribution of the dopant around titania particles and the incorporation of Ce atoms to anatase lattice denoted for the variation of "*a*" and "*c*" lattice parameter, **table 1**. Those facts effectively results in poor titania-titania connectivity necessary for early transformation to rutile. The remaining of anatase phase on MII and MIII materials is ascribed to the Ce atoms presence and it is in agreement with literature findings[47, 48]. The stabilization of TiO_2 in the anatase phase can usually be achieved by changing its bulk surface composition, and it is usual to add other atoms to titania to improve TiO_2 properties such as structural stability[47, 48]. It has been reported that CeO_2 has a property of stabilizing the active phase in a fine dispersed state and improving the resistance to thermal loss[49]. Using several techniques Cao *et al*.[47] proposed that Ti–O–Ce bonds formed in the Ce-doped samples enhanced the strength of the Ti–O bond and inhibited the phase transformation and particle coarsening. The wide peaks on Ce-TiO_2 materials compared with pure anatase would indicate the presence of particles with very small size in agreement with SEM images.

Besides the crystalline phase, the mechanical interlocking of micro- and nano- irregularities with the tissue plays an important role in bioactivity results. In order to evaluate the sample surface profiles, the surface roughness was analyzed. Using digitalized scanning electron microscopy (SEM) images, **figures 1 and 2**, and different software packages[26], the roughness arithmetical average deviation (R_a); the root mean square roughness (R_q), Kurtosis (R_{ku}) and Skewness (R_{sk}) coefficients were computed. The fractal architecture should also be assessed by calculating the 3D and 2D fractal dimensions (D_{2D}, D_{3D}). This concept is particularly interesting in surface and material science because natural fractals are repetitive patterns across a finite range of scales; and many biological structures, including bone, are fractal or even fractal-like. Each parameter is described in **ESI** and the obtained results are summarized in **table 2.** The five highest peaks and five deepest valleys averaged over the total surface are given by R_q; it is therefore, always bigger than the equivalent R_a measured for the same area. It can be seen that a decrease of R_q, R_a and fractal dimension values occurs from MI to MIII materials. The obtained D_{3D}

values are in accordance with three-dimensional fractal dimension of healthy trabecular bone obtained from high-spatial resolution magnetic resonance images[50]. R_{sk} and R_{ku} coefficients indicate the asymmetry of the surface; all materials present positive values of R_{sk} denoting the presence of profiles with more valleys than peaks[42]. The relationship between the number of peaks and valleys is given by the value of R_{ku}. Kurtosis coefficient describes the sharpness of the profile probability density. If $R_{ku} < 3$ the distribution curve is said to be platykurtoic and has relatively few high peaks and low valleys. If $R_{ku} > 3$ the distribution curve is said to be leptokurtoic and has relatively many high peaks and low valleys. All materials are platykurtoic; but the incorporation of Ce atoms seems to cause a slightly increase of the amount of valley on the material surface in comparison with pure TiO_2 material. The striped material (MII) presented the highest R_{ku} value in agreement with the existence of a major amount of valleys in its topography, **figure 2. Figure 4** displays the nitrogen adsorption-desorption isotherms and the corresponding BJH pore size distributions of all samples. The analysis of N_2 adsorption-desorption isotherms, **figure 4a**, indicated that all materials presented the typical Type IV isotherm with an H1 hysteresis loop (according to IUPAC classification[28]). This type of adsorption isotherm is typical for weak substrate–adsorptive interaction and cannot provide an accurate calculation of the inner surface area because changes of the adsorption characteristics after saturation by the first monolayer are not pronounced. Type H_1 hysteresis loops are often associated with pure mesoporous that contains non-intersecting mesopores of cylindrical geometry and similar size. Neither of the materials presents high surface areas or an ordered array of mesopores. The surface area BET (S_{BET}) just with the pore diameter (d_p) and volume (V_p) are summarized in **table 2**. One model pore size distribution is appreciated, except for MIII, in **figure 4b.** This fact indicate that no phase separation occurs during the assimilation of Ce atoms to TiO_2 matrix utilizing $Ce(Val)_3$ as precursor in contrast to what occurs with the incorporation of CeO_2 nanoparticles. Although from the study of the X-ray diffraction patterns of sample MIII can not be identified peaks related to CeO_2; the existence of a bimodal pore size distribution would be indicative of an incomplete incorporation of CeO_2 nanoparticles to the anatase matrix.

3.2 Bioactivity assays

3.2.1 Bone-like hydroxyapatite formation

Bioactivity is one of the most desirable properties of implants intended to be integrated into bone. A layer of bone-like hydroxyapatite (HA) forms on bioactive surface when it is implanted *in vivo* and acts as an intermediate layer between bone tissue and the implant[51]. As a consequence, bioactivity can be inferred, *in vitro,* if bone like HA is deposited on the surface of the investigated material in contact with

simulated body fluid (SBF)[32]. Also the ability to precipitate HA is an indication that the studied material prevents the development of a fibrous capsule, which is a negative event during the osseo-integration process. **Figure 5,** shows the SEM microphotographs of apatite coatings deposited on the studied materials after 1, 5, 10 days incubation in 1.5 SBF. All tested materials show a dense layer of HA crystals after 10 days of soaking. EDX microanalysis indicates that the Ca/P ≈ 1.60 which could be ascribed to stoichiometric HA, **ESI**. The theories concerning the bioactivity of crystalline TiO_2 are quite weak. The general consensus is that titanium oxide is bioactive because –OH groups are present on TiO_2 surfaces after being soaked in SBF [52, 53].These hydroxyl groups catalyze the HA precipitation. Uchida *et al*.[54] studied hydroxyapatite growth on diverse structured titania surfaces and provided an explanation of why the –OH groups on amorphous titania seems less effective than those on rutile and anatase. They indicated that for certain crystallographic planes in the crystalline titania structures, the oxygen positions match well with the –OH groups in hydroxiapatite crystal favoring epitaxial nucleation. Epitaxial growth of HA on rutile is expected to occur based on the two-dimesional similarity of the two crystal structures[52]. On the contrary, accordingly to Li *et al.*[55], HA is not biomimetically formed on single crystal TiO_2 anatase. One of the reasons given by the authors is that the density of –OH groups are not plentiful available at the appropriate crystal face. They also noted that while the individual crystals of dense anatase lack of bioactivity, porous anatase induces apatite deposition. In general, it is believed that a porous structure is capable of accelerating the biomimetic process[53]. The obtained materials showed bioactivity, regardless of its crystalline phases and the fact that they do not present high surface areas or an ordered array of mesopores, **table 2**. Subsequently, our results show that differences in crystals polymorphisms as well as porosity are not enough to induce bioactivity. Prior to the occurrence of bio-reactions that ensure bioactivity, some physicochemical processes must be thermodynamically possible. One of these events is that surface texture influences surface energy, which in turn, affects bio-reactivity[56]. Being the HA formation on TiO_2 in supersaturated aqueous solution is an heterogeneous nucleation process, according to the classical nucleation theory, the critical free energy (ΔG) depends on the supersaturation of the solution (S), the temperature (T), the net interfacial energy of nucleation (σ) and the particle surface area (A). Thus it is given by[56]:

$$\Delta G = -RT\ln(S) + \sigma A \qquad (3)$$

In this work TiO_2 samples were immersed in the SBF solution with a constant supersaturation with respect to HA and T; also no significant difference respect particles surface areas can be appreciated

between the materials. The only variation existing among materials is the net interfacial energy barrier given for the parameter (σ), which is highly dependent of both surface topography and the interfacial presence of highest polar components[56]. Consequently, we think that the HA phase nucleates heterogeneously with the effective participation of surface energy and topography. On rough surfaces as in our case, the valleys seem to be the preferential sites for the nucleation and growth of calcium phosphates, causing a reduction of R_a. Similarly surfaces with positive skewness favor Ca-rich phase's depositions. Topographical analysis indicates that the materials MII and MIII, which present the highest number of valleys, cause a major and a fast coverage on their surfaces with HA crystals. Other relevant result is that the layers of HA agglomerates reproduce the original topography of the surface, see **table 3**, preserving the roughness at the micrometric level.

Hydroxyapatite layers grown on different surfaces have fundamentally different appearance, **figure 6.** HA crystals that cover the surface of material MI grow as a dense layer with plate like crystallites growing side by side, while in materials MII and MIII the crystallites grow in bundles. Globules made up of several HA crystals were formed on the substrate surface. We assume that these differences are related to the preferential growth of hydroxyapatite crystals in contact with the crystalline phases of titanium dioxide. Thus, in the material MI the preferential growing direction points out from the surface due to the interaction with the (001) surface of rutile TiO_2 crystallites [52]. On the contrary, if the epitaxial growth of HA is preferentially on (110) anatase surface [52], as happens in materials MII and MIII, crystallites form spherical-like globules with 3-5 μm in diameter composed by agglomerates of plate-like nano-morphology crystals of ~ 150 nm length. The final morphology according to Kokubo *et al.* [4, 32]is essential for bone-bonding.

3.2.2 Osteoblast-material interaction

The biocompatibility of TiO_2-CeO_2 materials was confirmed by assessing their interactions with neonatal rat calvarian osteoblasts. The increase of CeO_2 concentration and the effect of HA layer micro-morphology on cell viability and adhesion were evaluated after 24, 48 and 72h of treatment by microscopic observation. When osteoblasts were seeded in the presence of materials with different ceria concentration ([CeO_2] = 0.05; 0.08 and 0.10 wt%), no significant changes were observed in cell adhesion or viability after 24 and 72 h of treatment in comparison with control, **table 4.** Similar results were obtained varying the material micro-morphology. During the process of adhesion and spreading in the presence of material, osteoblast morphology was similar to control for all tested samples; they showed their typical polygonal or widespread forms with fine filopodia and abundant surface folds,

figure 7. The obtained results exclude any negative effect of the material crystalline microstructure, morphology and CeO_2 presence in the osteoblast survival.

3.4 Isothermal Peroxynitrite ($ONOO^-$) decay

Much of the damage caused during the process of implantation is attributed to the presence of the $NO^{\bullet}$ and $O_2^{\bullet -}$ species released in physiological conditions by activated macrophages and neutrophils; their reaction *in vivo* conduces to peroxynitrite ion ($ONOO^-$) formation [57]. Given to its oxidizing power and nitrating activity, peroxynitrite is cytotoxic and is associated to inflammatory diseases[57]; consequently it is logical to test the material interaction with this highly reactive molecule. Peroxynitrite degradation was studied under two treatments conditions at 25ºC: by diluting 100µL of freshly prepared $ONOO^-$ solution in 900 µL of PBS (T1) and in 900 µL of triple-distilled water (T2). At the first conditions no significant effects regarded to the material presence was observed, **ESI**. We assume that the reaction is so fast that we fail to detect any effect related to material-peroxynitrite interaction. In T2, degradation of $ONOO^-$ is far slower, allowing us to observe a significant effect due to the CeO_2-TiO_2 materials presence. The biochemistry of $ONOO^-$ is very complicated due to the multiple possible reactions in the presence and absence of CO_2, H^+ and metals during its decomposition[14].

While peroxynitrous acid isomerizes to nitrate (reaction 4), the peroxynitrite anion does not.

$$ONOOH \rightarrow H^+ + NO_3^- \quad (4)$$

Decomposition of peroxynitrite anion is less well investigated and accordingly to Kissner and Koppenol [58]several types of reactions must be considered.

$$2\ HOONO \rightarrow 2\ HNO_2 + O_2 \quad (5)$$

$$HOONO + ONOO^- \rightarrow 2\ NO_2^- + O_2 + H^+ \quad (6)$$

$$2ONOO^- \rightarrow 2NO_2^- + O_2 \quad (7)$$

Since the pK_a of peroxynitrous acid is 6.8 (reaction 3) at an ionic strength of 0.1M and 25ºC[58], at work conditions (pH = 13.1 and $[ONOO^-]_0 > 0.1$ mM) peroxynitrite anion is the predominant specie present. After degradation the only form detected was nitrite anion, **figure 8**, therefore we assumed that bimolecular decomposition (reaction 7) mainly occurs and is certainly slower than reaction 6 in

agreement with Kissner and Koppenol [58]. Peroxynitrite and nitrite absorbs UV light at a wavelength of 302 nm and 354 nm respectively (ε_{302} = 1700 M^{-1} cm^{-133}, ε_{354} = 2500 M^{-1} cm^{-159}) thus peroxynitrite anion reactions can be measured kinetically using UV-spectroscopy. Based on this property, it was observed that all prepared material accelerated and change kinetic behavior of the completed conversion of peroxynitrite to nitrite ion after 3500 seconds in water at 25ºC, **figure 9a and 9b.** Kinetic parameters were calculated from the reaction rate dependence on concentration[60] and the obtained results were summarized in **table 5**. In MI and MII materials' presence, it can be observed an augment in the peroxynitrite anion reaction rate just with the kinetic order after an induction $ONOO^-$ concentration. Nevertheless, in contact of MIII the $ONOO^-$ degradation followed a second-order kinetic from the beginning of the experiment. Experimentally it was determined that degradation of peroxynitrine anion in absence of material occurred through a first-order reaction kinetic with a k_1 = $(1.27 \pm 0.07)\times 10^{-4}$ s^{-1}, **table 5**. The obtained constant rate value is similar than literature data obtained for peroxyacids decomposition[57]; however for such compounds the reaction order is of first order in both, the acid and its conjugate base. In the presence of materials MI and MII, degradation behaved as a first order kinetic process with a slightly increment of k_1, followed by a second-order kinetic transformation with a huge augment of k_2 that occurred at $[ONOO^-]$ = 1.47mM for MI and = 0.74 mM for MII. For MIII, induction period has not been detected and degradation always matched to a second-order kinetic process.

On basis of literature findings[14, 58] and peroxyacids decomposition[57], we adapted a putative mechanism to model our results.

$$2ONOO^- \rightarrow \text{INTERMEDIARY} \quad (8)$$

$$\text{INTERMEDIARY} \rightarrow 2NO_2^- + O_2 \quad (9)$$

We assume that for the degradation of peroxynitrite anion in absence of material, reaction 9 is the slowly step and the determining of the reaction rate. Thus, the reaction matches to a first-order kinetic equation. Materials interact with the intermediary species causing a rate dependence of reaction 8 with the consequent change into a second-order kinetic and the rate constant. The results suggest that the interaction with $ONOO^-$ is not specific upon the Ce ion in agreement with literature[14]. Even though all materials caused an increment of $ONOO^-$ degradation the presence of Ce ions provokes a transformation into a second order kinetic at a minor $ONOO^-$ concentration. By this way in the presence of MIII material, that content CeO_2 nanoparticles, it can not be detected an induction

concentration and the process followed always a second-order kinetic. In this case the effect on k_2 was smaller. Striped material, MII, merge the less induction concentration with the high augment of the constant rate. The precise molecular mechanism behind of each catalytic reaction has yet to be elucidated and it is the focus of our current research. The obtained results represent convincing preliminary evidence that the prepared nano-structured materials readily react with peroxynitrite ion or one of the reactive oxidants and radicals that are a results of the non-enzymatic breakdown of peroxynitrite.

Conclusion

In summary, we report a simple and controllable route for the synthesis of CeO_2-anatase striped material with high bioactivity, biocompatibility and $ONOO^-$ scavenging properties. Making use of a microemulsion droplet system as a chemical microreactor and $Ce(Val)_3$ as ceria precursor it was possible to manipulate the micro-droplets interfacial organization to obtain decahedral anatase TiO_2 nano-particles arranged in aligned fibers of 20μm length and 1μm diameter. The presence of Ce atom in TiO_2 crystalline lattice stabilized anatasa polymorph, and such fact had a marked influence on the material bioactivity. The epitaxial growth of HA is preferentially on (110) anatase surface and plate-like nano-morphology crystallites of ~ 150 nm length arranged in spherical-like globules with 3-5 μm in diameter. Such morphology, according to literature, is essential for bone-bonding. Simultaneously, the presence of CeO_2 affect the scavenging properties of TiO_2 transforming the $ONOO^-$ degradation into a second order kinetic reaction after a $ONOO^-$ induction concentration. Striped material combines the less induction concentration, the high augment of the $ONOO^-$ constant rate and the development of a hydroxyapatite layer of the specific morphology required for bone integration.

Acknowledgements:

The authors acknowledge Universidad Nacional del Sur (PGI 24/ZQ07), Concejo Nacional de Investigaciones Científicas y Técnicas de la República Argentina (CONICET, PIP-11220100100072.), Xunta de Galicia (Project 10PXIB206258PR). NLD, ANG and JLMB have doctoral and postdoctoral fellowships of CONICET. PVM and GS are researchers of CONICET.

Electronic Supplementary Information (ESI) Available:

Material structural characterization: XRD, EDX, nano-particles size distribution histograms. Description of micro-rough parameters, Bioactivity: HA layer characterization (Ca/P ratio, EDX

characterization), Giemsa stained of calvarian osteoblast after 72h of treatment in the presence of TiO_2 and TiO_2-CeO_2 materials. $ONOO^-$ degradation: degradation kinetic in PBS and determination of kinetic parameters.

References

1. W. Dong, T. Zhang, J. Epstein, L. Cooney, H. Wang, Y. Li, Y.-B. Jiang, A. Cogbill, V. Varadan and Z. R. Tian, *Chemistry of Materials*, 2007, **19**, 4454-4459.
2. M. M. Stevens, *Materials Today*, 2008, **11**, 18-25.
3. Fouda M.F.A. , Nemat A., Gawish A. and Baiuomy A.R., *Australian Journal of Basic and Applied Science*, 2009, **3**, 1122-1129.
4. T. Kokubo, H.-M. Kim and M. Kawashita, *Biomaterials*, 2003, **24**, 2161-2175.
5. Ma Z. , Kotaki M., Inai R. and Ramakrishna S., *Tissue Engineering* 2005, **11**, 101-109.
6. M. D. Rosenberg, *Science*, 1963, **139**, 411-411.
7. R. L. Price, K. Ellison, K. M. Haberstroh and T. J. Webster, *Journal of Biomedical Materials Research Part A*, 2004, **70A**, 129-138 and references therein.
8. N. Hassan, V. Verdinelli, J. M. Ruso and P. V. Messina, *Soft Matter*, 2012, **8**, 6582-6592.
9. K. M. Woo, V. J. Chen and P. X. Ma, *Journal of Biomedical Materials Research Part A*, 2003, **67A**, 531-537.
10. T.P. Dalton, H. G. Shertzer and A. Puga, *Ann. Rev. Pharmacol. Toxical.*, 1999, **39**, 67-1010.
11. J. Dissemond, M. Govs and S. N. Wagner, *Hautzart*, 2002, **53**, 718-723.
12. C. K. Sen, *Wound Rep. Feg.*, 2003, **11**, 431-438.
13. A.S. Karatoki, N.A. Monteiro-Riviere, R. Aggarwal, J.P. Davis, R.J. Narayan, W.T. Self, J. McGinnis and S. Seal, *Biol. Mat. Sci.*, 2008, 33-37.
14. J. Dowding, S. Seal and W. Self, *Drug Deliv. and Transl. Res.*, 2013, 1-5.
15. I. Batinić-Haberle, in *Methods in Enzymology*, ed. P. Lester, Academic Press, 2002, pp. 223-233.
16. B. J. Day, I. Fridovich and J. D. Crapo, *Archives of Biochemistry and Biophysics*, 1997, **347**, 256-262.
17. E. G. Heckert, A. S. Karakoti, S. Seal and W. T. Self, *Biomaterials*, 2009, **29**, 2705-2709.
18. D. Schubert, R. Dargush, J. Raitano and S. W. Chan, *Biochem. Biophys. Res. Commun.* , 2006, **342**, 86-91.
19. M. Das, S. Patil, N. Bhargava, J. F. Kang, L.M. Riedel and S. Seal, *Biomaterials* 2007, **28**, 1918-1925.
20. J. Niu, A. Azfer, L. M. Rogers, X. Wang and P. E. Kolattukudy, *Cardiovasc. Res.*, 2007, **73**, 549-559.
21. J. Chen, *Nature Nanotech*, 2006, **1**, 142-150.
22. Messina P.V., Verdinelli V., Pieroni O. and Ruso J.M., *Colloid Polym Sci*, 2013, **291** 835-844 and references therein.
23. J. M. Ruso, A. N. Gravina, N. L. D'Elia and P. V. Messina, *Dalton Transactions*, 2013, **42**, 7991-8000.
24. N. Hassan, V. Verdinelli, J. M. Ruso and P. V. Messina, *Langmuir*, 2011, **27**, 8905-9812.
25. A. Bumajdad, J. Eastoe and A. Mathew, *Advances in Colloid and Interface Science*, 2009, **147–148**, 56-66.
26. N. Ibaseta and B. Biscans, *Powder Technology*, 2010, **203**, 206-210.
27. B. C. Lippens, B. G. Linsen and J. H. d. Boer, *Journal of Catalysis*, 1964, **3**, 32-37.

28. K. S. W. Sing, D. H. Everett, R. A. W. Haul, L. Moscou, R. A. Pierotti, J. Rouquérol and T. Semieniewska, *Pure & Appl. Chern.*, 1985, **66**, 1739-1758.
29. E. P. Barrett, L. G. Joyner and P. P. Halenda, *Journal of the American Chemical Society*, 1951, **73**, 373-380.
30. Mohapatra P, Mishra T and P. KM, *Appl Catal Gen*, 2006, **310**.
31. Spurr R A and Myers H, *Anal Chem*, 1957, **29**, 760-762.
32. T. Kokubo, H. Kushitani, S. Sakka, T. Kitsugi and T. Yamamuro, *Journal of biomedical materials research*, 1990, **24**, 721-734.
33. J. S. Beckman, J. Chen, H. Ischiropoulos and J. P. Crow, in *Methods in Enzymology*, ed. P. Lester, Academic Press, 1994, pp. 229-240.
34. A. Saha, S. Goldstein, D. Cabelli and G. Czapski, *Free Radical Biology and Medicine*, 1998, **24**, 653-659.
35. C. Quijano, D. Hernandez-Saavedra, L. Castro, J. M. McCord, B. A. Freeman and R. Radi, *Journal of Biological Chemistry*, 2001, **276**, 11631-11638.
36. G.W. Snedecor and W. G. Cochran, *sixth ed.Ames: Iowa State University Press, Iowa*, 1967.
37. N. L. D'Elía, A. N. Gravina, J. M. Ruso, J. A. Laiuppa, G. E. Santillán and P. V. Messina, *Biochimica et Biophysica Acta (BBA) - General Subjects*, 2013, **1830**, 5014-5026.
38. L. Qi, *Encycl. Surf. & Colloid Sci.*, 2006, 6183-6207 and references therein.
39. M. A. López-Quintela, C. Tojo, M. C. Blanco, L. García Rio and J. R. Leis, *Current Opinion in Colloid & Interface Science*, 2004, **9**, 264-278.
40. B. E. Yoldas, *J. Mat. Sci.*, 1986, **21**, 1087-1092.
41. J.-K. Park, J.-J. Myoung, J.-B. Kyong and H.-K. Kim, *Bull. Korean Chem. Soc.*, 2003, **24** 671-673.
42. P. S. Vanzillotta, M. S. Sader, I. N. Bastos and G. de Almeida Soares, *Dental Materials*, 2006, **22**, 275-282.
43. J. M. Ruso, V. Verdinelli, N. Hassan, O. Pieroni and P. V. Messina, *Langmuir*, 2013, **29**, 2350-2358.
44. A. Pärssinen, P. Elo, M. Klinga and M. T. Leskelä, *Rep. Inorg. Chem. Commun.*, 2006, **9**, 856-859.
45. F. Porta, L. Prati, M. Rossi and G. Scari, *Colloids Surf, A Physicochem Eng Asp*, 2002, **211**, 43-48.
46. F. Dachile, P. Y. Simons and R. Roy, *The American mineralogist.*, 1968, **53**, 1929-1939.
47. X. P. Cao, D. Li, W. H. Jing, X. W. H and F. Y. Q, *J. Mat. Chem.*, 2012, **22**, 15309–15315.
48. T. López, F. Rojas, R. Alexander-Katz, F. Galindo, A. Balankin and A. Buljan, *Journal of Solid State Chemistry* 2004, **177**, 1873-1885.
49. P. Periyat, K. V. Baiju, P. Mukundan, P. K. Pillai and K. G. K. Warrier, *J Sol-Gel Sci Technol*, 2007, **43**.
50. A. Alberich-Bayarri, L. Marti-Bonmati, M. A. Perez, R. Sanz-Requena, J. J. Lerma-Garrido, G. Garcia-Marti and D. Moratal, *Medical Physics*, 2010, **37**, 4930-4937.
51. J. Forsgren, F. Svahn, T. Jarmar and H. Engqvist, *Acta Biomaterialia*, 2007, **3**, 980-984.
52. F. Lindberg, J. Heinrichs, F. Ericson, P. Thomsen and H. Engqvist, *Biomaterials*, 2008, **29**, 3317-3323.
53. M. Wen, J.-F. Gu, G. Liu, Z.-B. Wang and J. Lu, *Crystal Growth & Design*, 2007, **7**, 2400-2403.
54. M. Uchida, H.-M. Kim, T. Kokubo, S. Fujibayashi and T. Nakamura, *Journal of Biomedical Materials Research Part A*, 2003, **64A**, 164-170.
55. P. Li, C. Ohtsuki, T. Kokubo, K. Nakanishi, N. Soga and K. de Groot, *Journal of biomedical materials research*, 1994, **28**, 7-15.

56. X. B. Chen, Y.-C. Li, P. D. Hodgson and C. Wen, *Acta Biomaterialia*, 2009, **5**, 2290-2302 and references therein.
57. C. Molina, R. Kissner and W. H. Koppenol, *Dalton Transactions*, 2013, **42**, 9898-9905.
58. R. Kissner and W. H. Koppenol, *Journal of the American Chemical Society*, 2001, **124**, 234-239.
59. N. Gayathri and N. Balasubramanian, *Analusis*, 1999, **27**, 174-180.
60. P. Atkins and J. d. Paula, eds., *Química Física*, Editorial Medica Panamericana, 2008.

Figure Captions

Figure 1. SEM microphotographs of prepared TiO_2 (MI) and Ce-TiO_2 (MII and MIII) materials. Scale bars correspond to 200 nm.

Figure 2. SEM microphotographs of Ce-TiO_2 materials showing striped (MII) and non-defined (MIII) morphologies. Scale bars correspond to 2 μm.

Figure 3. H-TEM microphotograph of sample MII.

Figure 4. (**a**) N_2 adsorption-desorption isotherms and (**b**) pore size distribution of synthesized materials.

Figure 5. SEM microphotographs of HA coatings deposited on the studied materials after 1, 5, 10 days incubation in 1.5 SBF at 37ºC. Scale bars correspond to 1μm.

Figure 6. SEM microphotographs of HA coatings deposited on MI (anatase-rutile phases) and MII (pure anatase phase) after 10 days incubation in 1.5 SBF at 37ºC.

Figure 7. Microphotograph of Giemsa stained osteoblasts after 72h of treatment in contact with material MII.

Figure 8. $ONOO^-$ spectra before and after degradation in presence of MII at T= 25ºC and pH = 13.1

Figure 9. Time evolution of $ONOO^-$ degradation and in presence and in absence of synthesized materials at T = 25ºC and pH = 13.1.

Scheme 1. Schematic representation of the synthesis conditions of the striped Ce-TiO_2 material (MII).

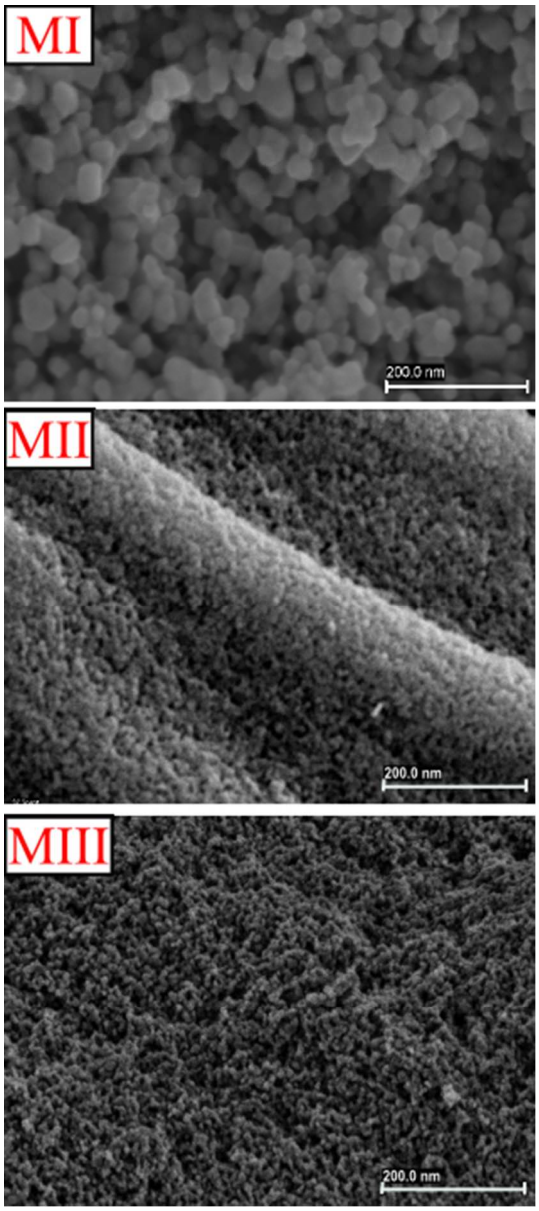

Figure 1. SEM microphotographs of prepared TiO2 (MI) and Ce-TiO2 (MII and MIII) materials. Scale bars correspond to 200 nm.

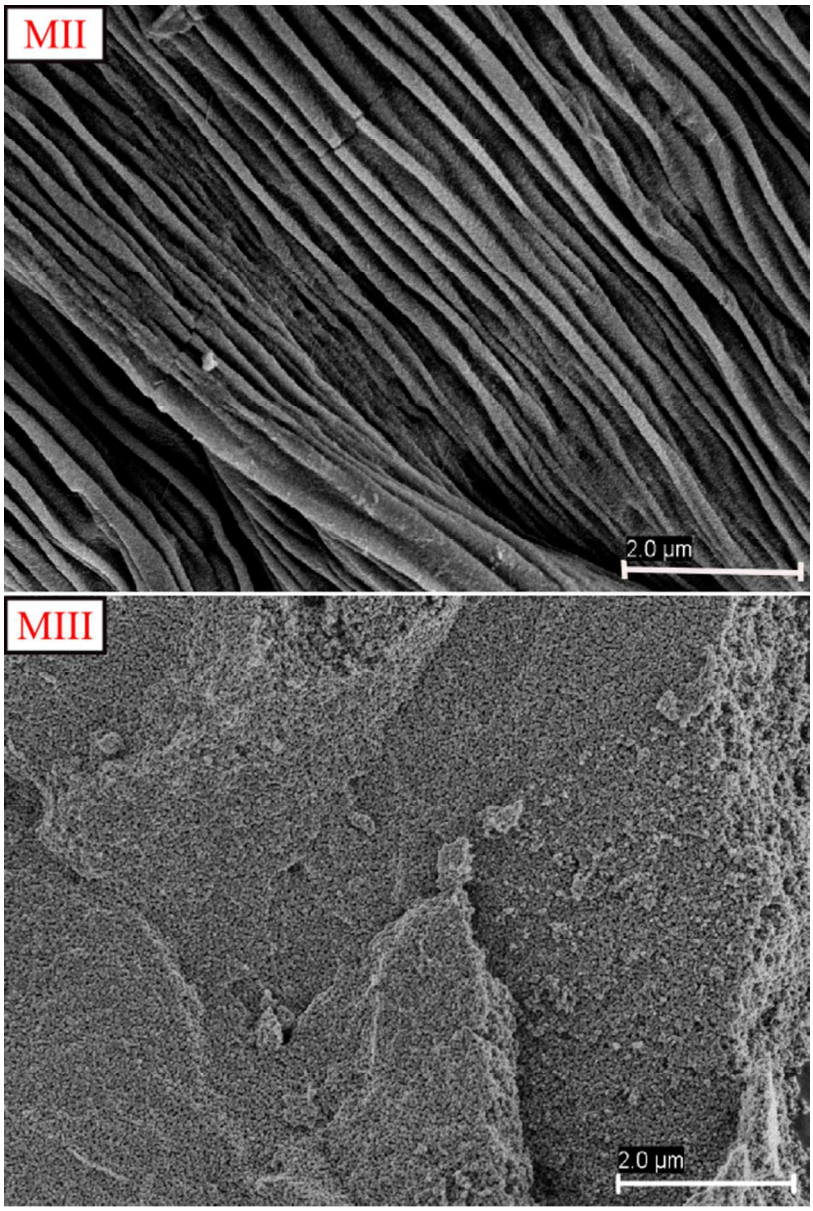

Figure 2. SEM microphotographs of Ce-TiO2 materials showing striped (MII) and non-defined (MIII) morphologies. Scale bars correspond to 2 µm.

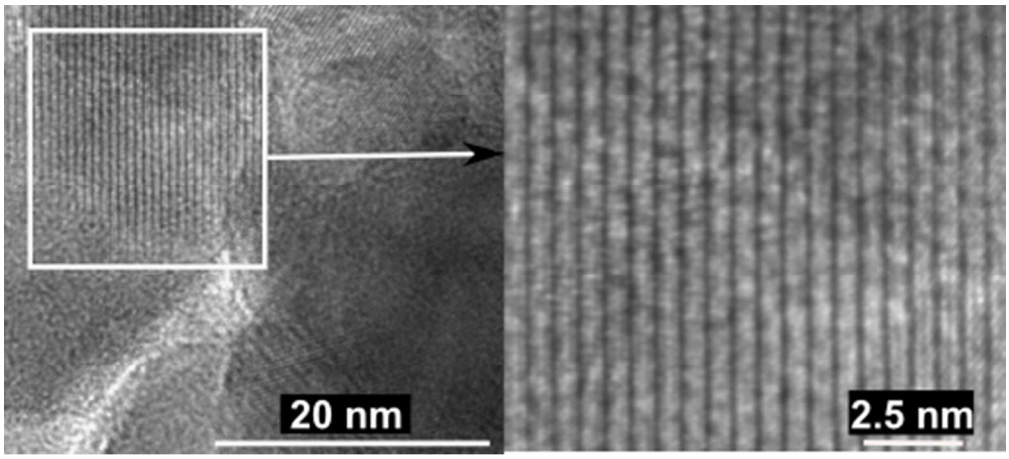

Figure 3. H-TEM microphotograph of sample MII.

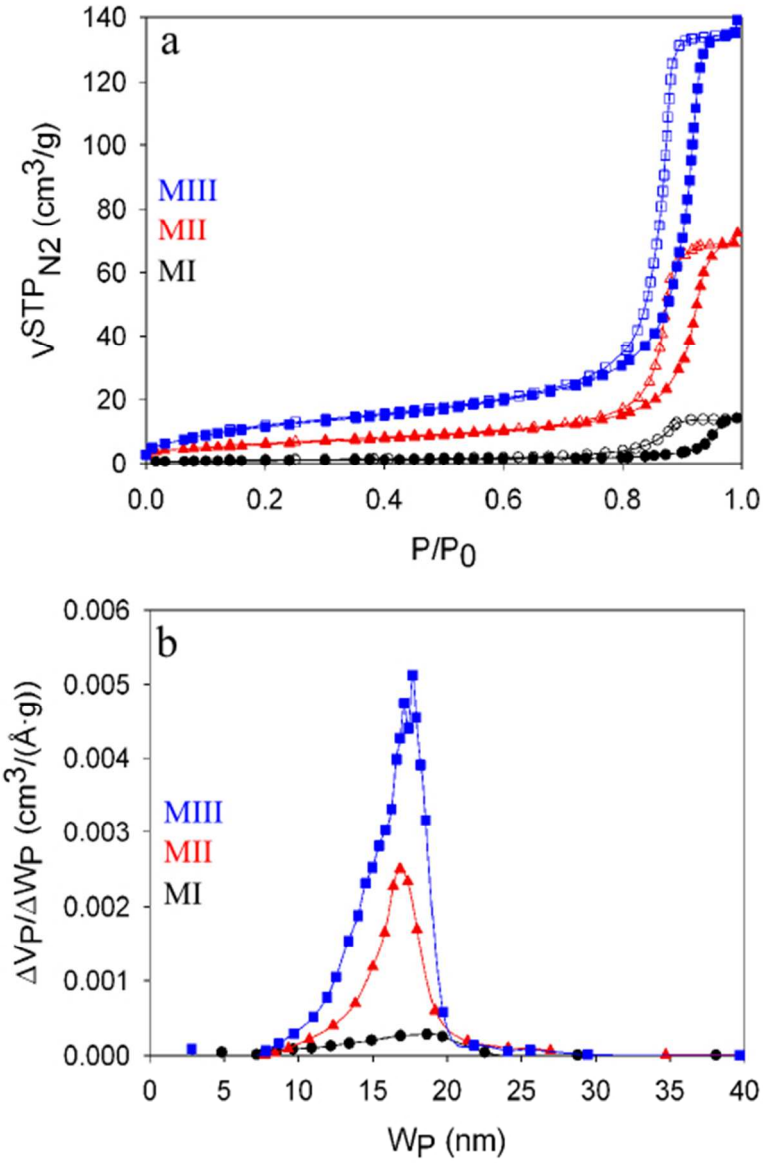

Figure 4. (a) N2 adsorption-desorption isotherms and (b) pore size distribution of synthesized materials.

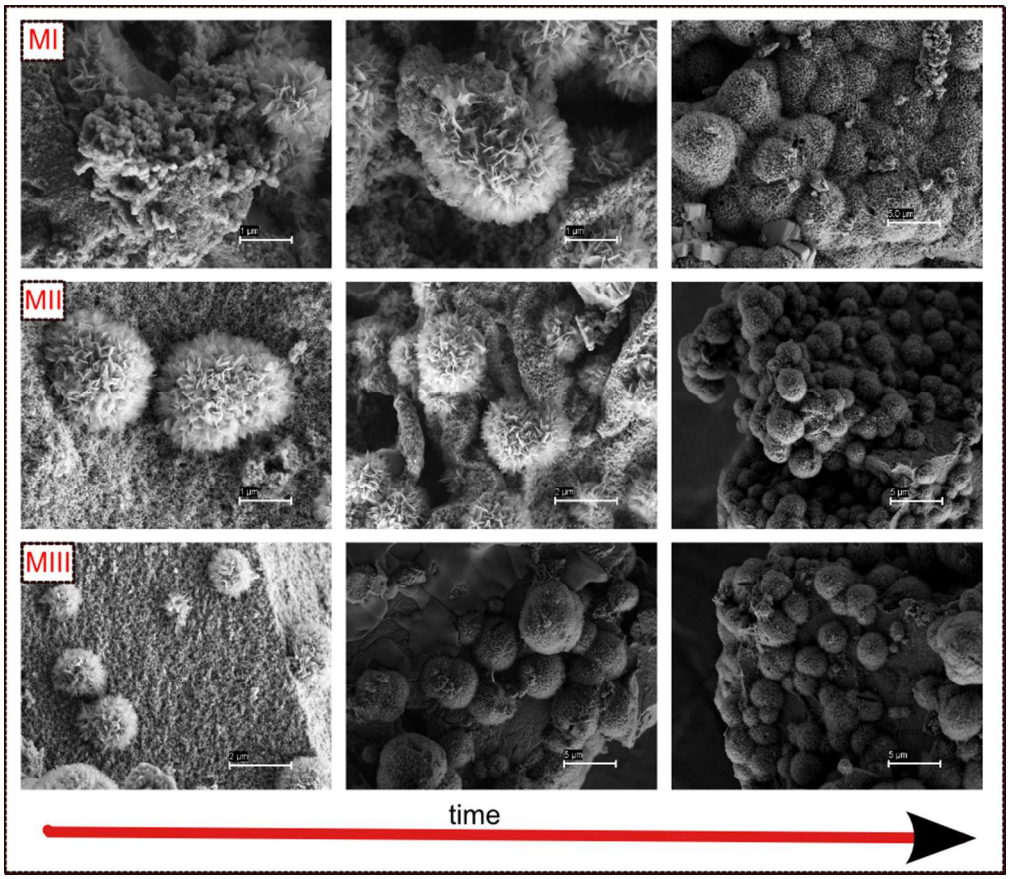

Figure 5. SEM microphotographs of HA coatings deposited on the studied materials after 1, 5, 10 days incubation in 1.5 SBF at 37ºC. Scale bars correspond to 1µm.

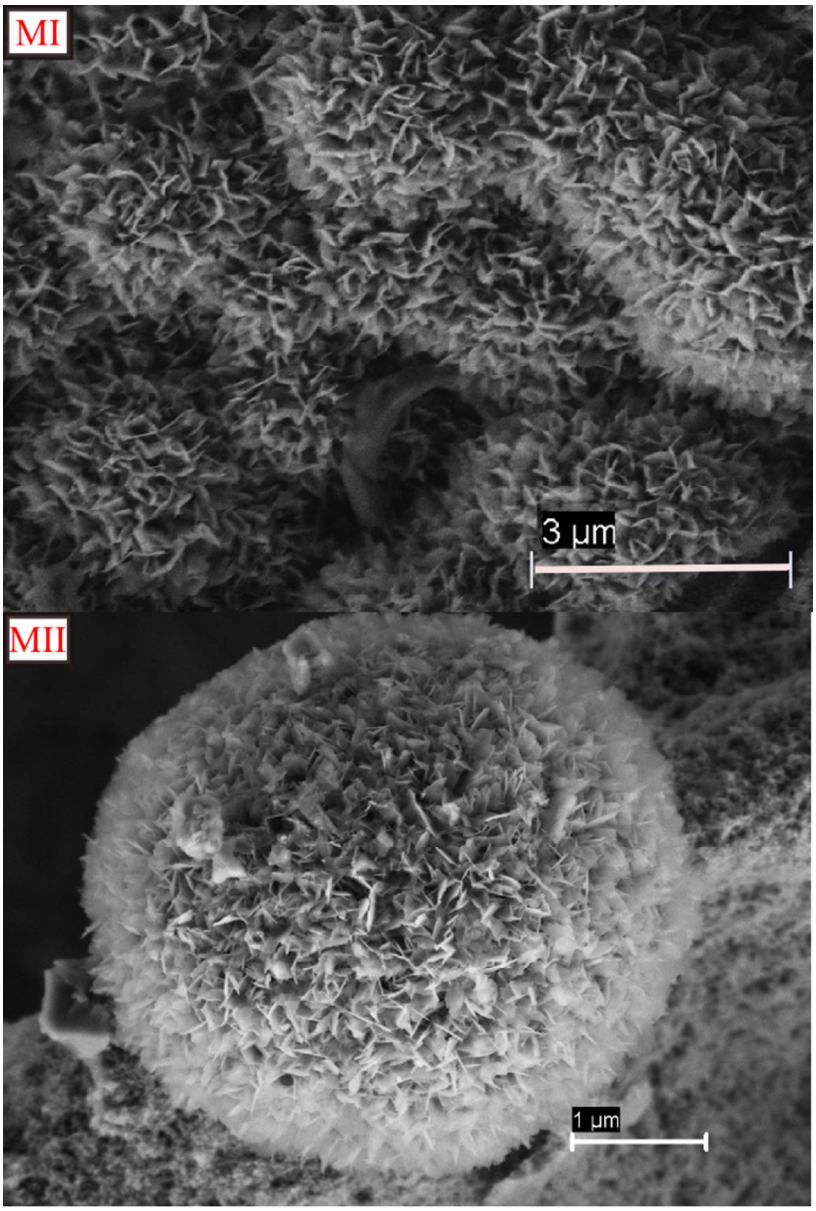

Figure 6. SEM microphotographs of HA coatings deposited on MI (anatase-rutile phases) and MII (pure anatase phase) after 10 days incubation in 1.5 SBF at 37ºC.

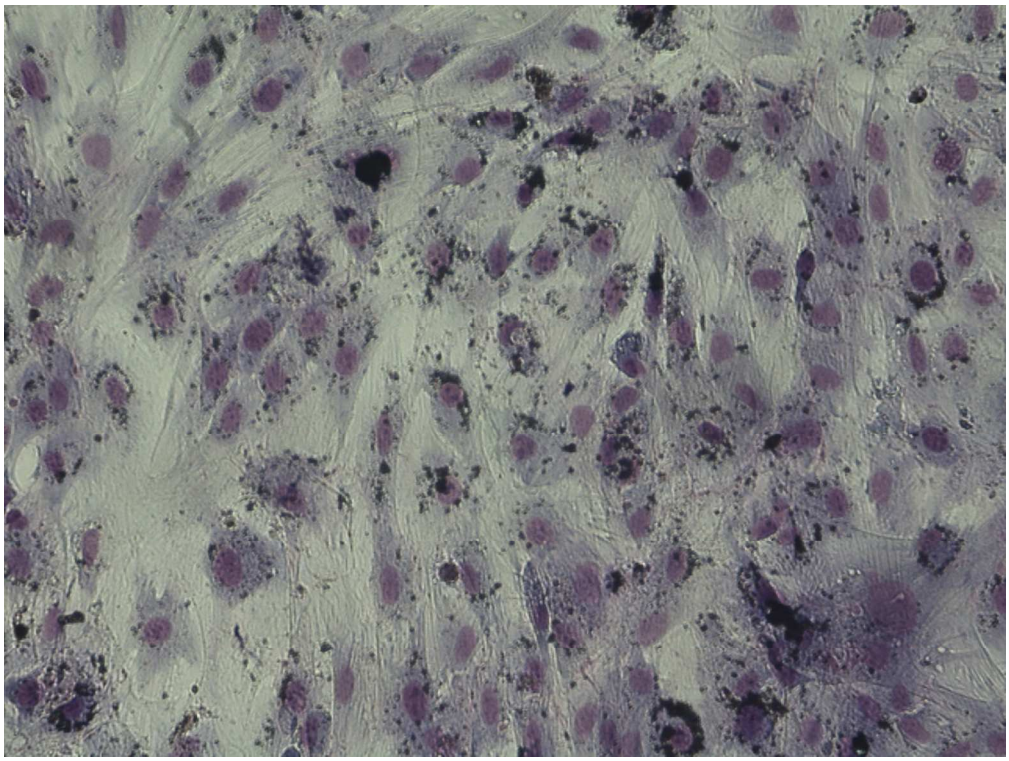

Figure 7. Microphotograph of Giemsa stained osteoblasts after 72h of treatment in contact with material MII.

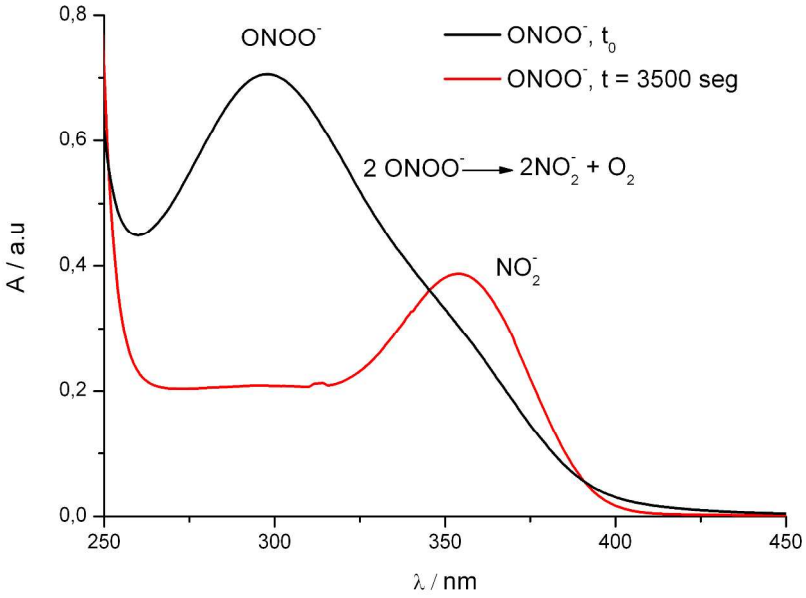

Figure 8. ONOO- spectra before and after degradation in presence of MII at T= 25ºC and pH = 13.1

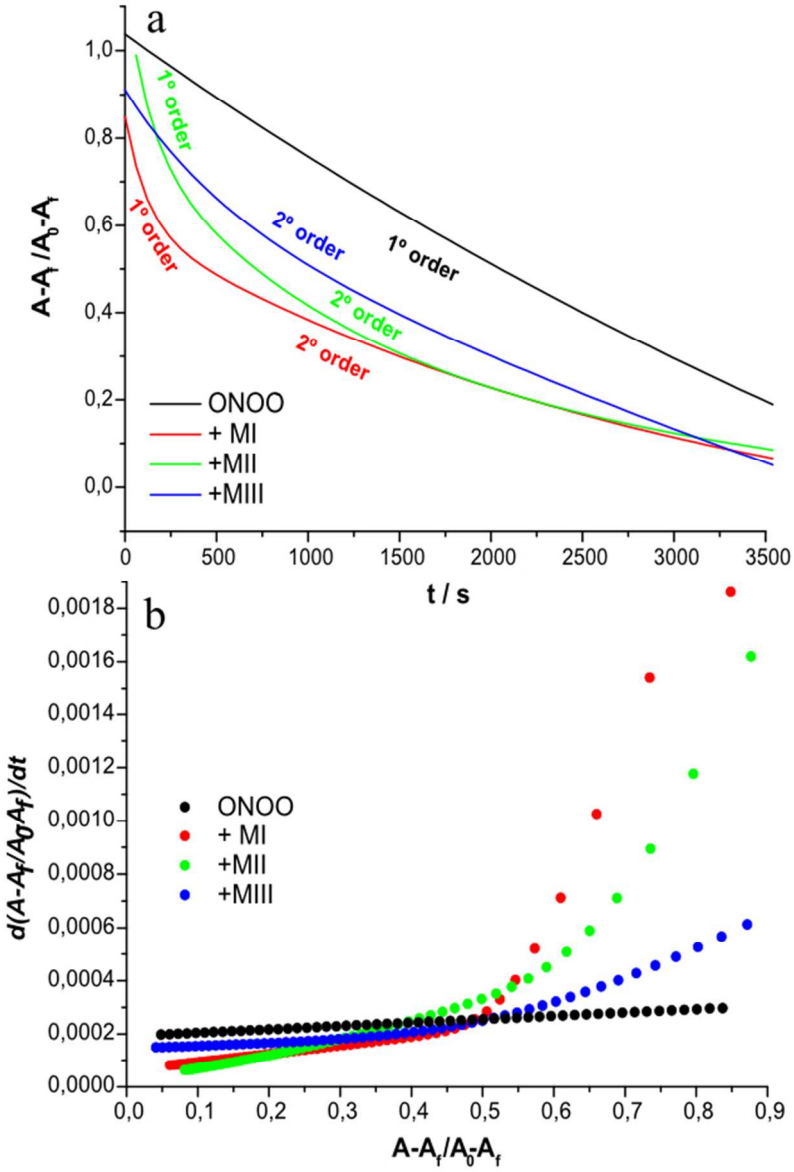

Figure 9. Time evolution of ONOO- degradation and in presence and in absence of synthesized materials at T = 25ºC and pH = 13.1.

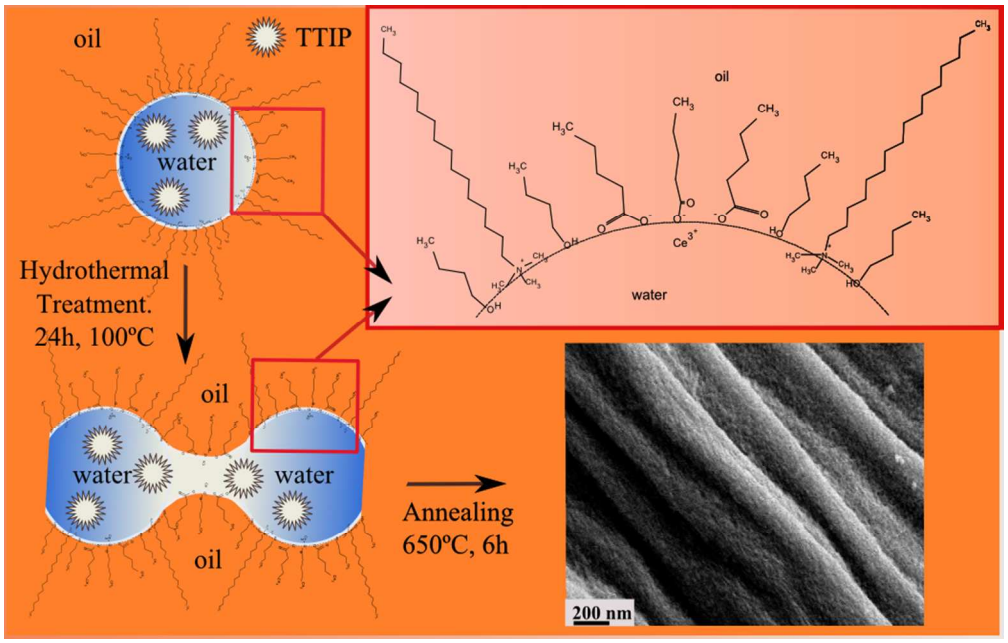

Scheme 1. Schematic representation of the synthesis conditions of the striped Ce-TiO2 material (MII).

Table 1 Crystalline characteristic of TiO_2 and Ce-TiO_2 materials

	Morphology	Cerium source	δ / nm	F_r%	a^*/Å	c^*/ Å
MI	Particulate		40	48	3.775	9.299
MII	Striped	$Ce(Val)_3$	34	0	3.785	9.465
MIII	Particulate	CeO_2 nanoparticles	28	0	3.785	9.463

(*) computed for anatase lattice

Table 2 Surface characteristic of TiO_2 and Ce-TiO_2 materials

	D_{2D}	D_{3D}	R_q/ nm	R_a/ nm	R_{sk}/ nm	R_{ku}/ nm	S_{BET}/m^2g^{-1}	d_p / nm	V_p/cm^3g^{-1}
MI	1.978	2.709	100.97	93.77	1.18	1.51	3	17	0.01
MII	1.968	2.705	79.35	63.96	1.44	2.28	21	19	0.10
MIII	1.928	2.686	64.42	56.06	1.33	1.97	43	19	0.21

Table 3 Physical-chemical characteristics of Ca-P coatings on TiO_2 and Ce-TiO_2 materials

	Coating Micro-morphology	Ca/P	D_{2D}	D_{3D}	R_q / nm	R_a / nm	R_{sk} / nm	R_{ku} / nm
M I	Dense layer of plate-like crystallites	1.63	1.747	2.601	70.87	61.58	1.41	2.27
M II	Spherulitic-like layer	1.62	1.809	2.630	60.09	45.43	1.80	3.97
M III	Spherulitic-like layer	1.60	1.804	2.627	50.77	41.47	1.55	2.86

Table 4 Effect of ceria concentration and HA coating micro-morphology on osteoblast viability.

			% of osteoblast viability	
	[CeO_2] wt%	HA Coating Micro-morphology	after 24 h treatment	after 72 h treatment
Control			99.12 ± 0.62	99.50 ± 0.50
	0.05		98.70 ± 0.35	98.81 ± 0.70
	0.08		99.06 ± 0.52	98.83 ± 0.23
	0.10		98.05 ± 0.33	98.87 ± 0.05
	0.08	Spherulitic-like layer	99.61 ± 0.52	98.83 ± 0.23

Table 5 Kinetic parameters of $ONOO^-$ degradation

	[$ONOO^-$] range	**k_1 / s^{-1}**	**R^2**	**n**	**[$ONOO^-$] range**	**k_2 / $mM^{-1}s^{-1}$**	**R^2**	**n**
$ONOO^-$	0 – 1.52 mM	$(1.27 \pm 0.04)\times10^{-4}$	0.9999	1				
+ M I	0 – 1.47 mM	$(3.35 \pm 0.07)\times10^{-4}$	0.9987	1	1.47 – 1.52 mM	(0.064 ± 0.017)	0.9989	2
+M II	0 – 0.74 mM	$(6.14 \pm 0.09)\times10^{-4}$	0.9998	1	0.74 – 1.52 mM	(0.068 ± 0.013)	0.9997	2
+M III					0 – 1.52 mM	(0.012 ± 0.022)	0.9969	2